Chemical routes to materials

Photovoltaic performance of non-covalent functionalized single-layer graphene in dye-sensitized solar cells (DSSCs)

Erdal Igman[1,2,*] , Ozkan Bayram[1,2,3], Ahmet Mavi[4], Ugur Cem Hasar[5], and Onder Simsek[6]

[1] Department of Material Science and Nanotechnology Engineering, Bayburt University, TR-69100 Bayburt, Turkey
[2] Graduate School Natural and Apply Science, Department Nanoscience and Nanoengineering, Ataturk University, TR-25240 Erzurum, Turkey
[3] Central Application and Research Laboratory (BUMER), Bayburt University, TR-69100 Bayburt, Turkey
[4] Department of Chemistry Education, Ataturk University, TR-25240 Erzurum, Turkey
[5] Electrical and Electronics Eng. Department, University of Gaziantep, TR-27310 Gaziantep, Turkey
[6] Central Application and Research Laboratory (MERLAB), Agri Ibrahim Cecen University, 04100 Agri, Turkey

ABSTRACT

In this study, it was aimed to fabricate new effective alternative counter electrodes (CEs) in dye-sensitized solar cells (DSSCs). For this purpose, firstly, single-layer graphene (SLG) thin films were grown by chemical vapor deposition (CVD) method. Then, these films were separately functionalized with 1,8-cineole (ppCin/SLG), D-Limonene (ppLim/SLG) and Thiophene (ppTh/SLG) by plasma polymerization. Number of layers in CVD-grown graphene determined by Raman, transmission electron microscope (TEM) and ultraviolet–visible (UV–Vis) spectroscopy. Chemical structures of plasma polymerised (pp) thin films were investigated by Fourier transform infrared (FTIR) spectroscopy. Photovoltaic parameters of DSSCs were calculated, and electrocatalytic properties of CEs were investigated by electrochemical impedance spectroscopy (EIS). Polymer functionalization greatly enhanced the electrical conductivity and electrocatalytic activity properties of graphene compared to that of SLG. The efficiencies of DSSCs with ppCin/SLG and ppLim/SLG CEs were 1.10% and 1.02%, respectively. As a result, the cell efficiencies of ppCin/SLG and ppLim/SLG could be as alternative materials to platinum (Pt) counter electrode.

2 Springer

Introduction

Since first fabricated in 1991 [1], dye-sensitized solar cells (DSSCs) have attracted the attention of many researchers for their advantages such as easy fabrication, low production cost, environmentally friendly and relatively high cell efficiency [2]. In general, DSSCs consist of a dye-sensitized semiconductor photoanode, an iodide/triiodide electrolyte solution and a counter electrode (CE). Platinum (Pt) electrodes with high electrocatalytic activity and electrical conductivity are generally used as CE in DSSCs [3]. Due to its high cost, depletion resources in nature and poor corrosive behavior to the redox solution containing I^-/I^{3-} [4], counter electrode material that may be an alternative to platinum counter electrode (PtCE) have been intensively explored by researchers recently.

Many metal oxide [5], sulfur [6], selenint [7], carbon nanoparticles [8], carbon nanotubes [9] and graphene nanostructures [3, 10] are the most remarkable of these studies. However, the energy efficiency of the PtCE has not yet been achieved using these counter electrodes. In particular, it is of great importance to improve their electrical conductivity and electrocatalytic activity in order to increase the energy efficiency of carbon-based counter electrodes [11]. Graphene, which is carbon-based structure, is particularly noteworthy due to the potential of its electrocatalytic activity and electrical conductivity. The catalytic activity of graphene is known to be enhanced by some oxygen-containing functional groups such as hydroxyls, epoxides, carboxyls and carbonyls [2]. In the literature, it has been reported that polyaniline (PANI), poly3, 4-ethylenedioxythiophene (PEDOT) and similar polymer/graphene nanocomposite structures are used as counter electrodes [2–4, 12–16]. Wang et al. [17] synthesized polyaniline–graphene/graphene oxide (PANI-G/GO) multipanel CEs to increase the compatibility of the I^-/I_3^- redox species with the counter electrode and investigated the effect of PANI and graphene binding by covalent bonds on the cell efficiency. They reported that superior electrocatalytic activity and electrical conductivity, which they believed to be caused by the multilayered structure, significantly improved the cell efficiency of DSSCs. The efficiency obtained by using PANI/graphene multilayer CEs in DSSC was determined as 7.88%. Shadid et al. [18] produced polymer functionalized nanocomposites for use as a counter electrode in DSSC cells. They performed the functionalization by synthesizing PANI on several layers of graphene. Power conversion efficiency (PCE) of Gr/PANI nanocomposite and PtCE was determined as 3.58% and 3.97%, respectively. Lee et al. [19] developed PEDOT/graphene counter electrode material without using Pt and transparent conducting oxide (TCO) and investigated their photovoltaic performance in DSSC applications. The high conductivity of PEDOT films and the superior electron transport property of graphene were considered an important factor in the nanocomposite design process, and this was believed to be an alternative to the Pt electrode. Platinum-free counter electrode material provided an energy conversion efficiency of 6.26%, while the cell efficiency obtained using conventional Pt was determined as 6.68%. In this study, we aimed to develop alternative counter electrode material that is well compatible with the hexagonal structure of graphene using some essential oil components obtained from organic compounds. Due to the hexagonal structure of the monomer, the production of electrodes with a large surface area will be realized and it is also aimed to increase the electrocatalytic activity due to some functional groups of the polymer obtained from these essential oils. By functionalizing graphene using various polymers, functional groups such as carboxyl and hydroxyl will be produced and these groups will facilitate further interaction of the triiodide ions with the electrode by causing defects between the Graphene/Polymer counter electrode and triiodide used as a catalyst in DSSC. With increasing interaction, electron transport will be increased and cell efficiency of Graphene/Polymer nanocomposite electrodes will be improved.

Improving the battery efficiency of DSSC cells is possible with a counter electrode with good electrocatalic activity and good electron transfer, as well as a photoanode that will facilitate the transport of the excited electron. Recently, it is widely used in ZnO and TiO_2 as photoanode materials due to these superior properties. TiO_2 has been investigated by many researchers as a photoanode material in DSSCs due to its superior optical and electronic properties, such as its large surface area and dye loading potential. In particular, one-dimensional titanium nanotubes (TNTs) are more potential due to their long electron paths and fast electron transport.

The most important aim of this study is to produce a new material alternative to Pt which is used as traditional electrode material in DSSC cells. There are many studies in the literature on the production of alternative electrode materials based on polymer and graphene and even their derivatives. However, in this study, it is aimed to produce a new candidate material by using both the superior electrical properties of graphene and the composition of the polymer's superior compatibility with the electrolyte. As a result, the use of Graphene/Polymer nanocomposite cell, which has both superior electrocatalytic activity and large surface area, in DSSC cells and its effect on cell performance will be investigated.

Experimental procedures

Growth of the TiO₂ nanotube arrays

TiO$_2$ nanotube arrays were grown by anodic oxidation of titanium foils (0.25 mm thick, 99.7% purity, Sigma-Aldrich) in an electrolyte containing ethylene glycol, 0.4%wt NH$_4$F and 5%wt deionized (DI) water. Anodization voltage of 40 V was applied for 2 h. Later, in order to convert from amorphous to anatase phase, as-grown TiO$_2$ nanotube arrays were annealed at 450 °C for 1 h in air ambient [20].

Growth of graphene thin films

SLG thin films were grown on Cu foils (Alfa-Aesar; 25 μm thick, purity 99.8%) by CVD method as indicated in our previous studies [21]. The schematic diagram of the CVD system is given in Fig. 1. CVD system consists of main parts such as monomer inlet unit, Radio Frequency (RF) matching unit, vacuum chamber, vacuum pump and pressure gage. The monomer inlet provides the purpose of leaking the monomer material to the area where coating can be made, namely the vacuum chamber with the help of the sensitive valve. The RF unit is used to break up the monomer leaked into the vacuum chamber by applying energy with a frequency of 13.56 MHz between two electrodes. The vacuum pump is widely used to reduce the pressure of the vacuum medium to the desired value, and the pressure of the environment is determined with the help of the vacuum gage. Pieces of Cu foils (2.5 cmx2.5 cm) were precleaned in acetone, isopropanol (IPA) and DI water for 5 min each and then dried with nitrogen gas [22]. After precleaning of Cu foils, they were placed on the sample holder of the CVD system (Nanovak Co. Turkey), and the base pressure was reduced to 5m Torr by means of the vacuum pump. Then, the Cu foils were heated to ~ 1000 °C with a heating rate of ~ 25 °C/min and annealed for 30 min in hydrogen (H$_2$) ambient with a flow rate of 20 sccm. To synthesize graphene films, the CVD reactor was supplied with 10 sccm of CH$_4$ and 10 sccm of H$_2$ for 30 min. The graphene growth process was performed at a total pressure of 1 Torr.

Finally, graphene films were cooled down to room temperature with a cooling rate of 12.5 °C /min and in H$_2$ ambient with a flow rate of 20 sccm.

Transfer of graphene thin films

As-grown graphene film on Cu foil was transferred onto fluorine-doped tin oxide (FTO; Rs < 10 ohms/sq) substrates using polymethyl methacrylate (PMMA) method [21, 23]. Firstly, PMMA thin film was spin-coated on graphene film, and then Cu substrate was etched away by an aqueous solution of

Figure 1 Schematic diagram of RF-PECVD system [24].
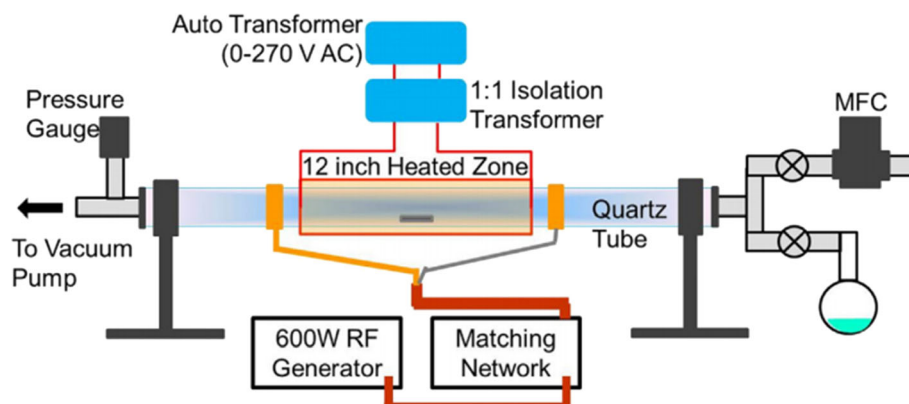
iron trichloride for 2 h. After that, the PMMA/-graphene stack was rinsed with DI water three times for 10 min each and transferred onto the FTO substrate. After the drying PMMA/graphene/FTO on a hot plate, PMMA film was removed by dissolving with acetone. Finally, graphene onto FTO was dried with nitrogen gas.

Functionalization of CVD-grown graphene

Graphene thin films were functionalized by the plasma enhanced chemical vapor deposition (PECVD) technique using 1,8-cineol, D-Limonene and Thiophene monomers. Firstly, graphene samples, transferred to FTO, were placed on the sample holder, and the base pressure of the system was reduced to 5m Torr thanks to the vacuum pump. Secondly, the monomer (1,8-cineol, D-Limonene and Thiophene) was sent to the vacuum chamber, and plasma ambient was obtained by applying RF power [25–28]. Each experiment was carried out at deposition time of 5 min, at RF power of 20 W and total pressure of about 500m Torr. Finally, RF power cut off, vacuum pump switched off and the system switched on to atmosphere ambient. Thus, graphene/polymer nanocomposites as counter electrodes for DSSCs were obtained.

Assembling of DSSCs

TiO_2 nanotube (TNT) arrays were coated with ruthenium (Ru)-based commercial N719 dye (Sigma-Aldrich) for 24 h to fabricate photoanodes. Then, a 60 μm thick Surlyn sealant (Solaronix, active cell area 0.196 cm^2) was placed between dye coated TiO_2 thin film and graphene/polymer counter electrode [20].

Characterization of DSSC

TNTs were characterized by XRD and SEM analysis. The presence of the anatase phase by XRD and the length and diameter of the nanotubes were investigated by SEM analysis. Graphene nanosheets were examined by Raman, TEM and UV–Vis analyzes. The number of layers was investigated by Raman, UV–Vis and TEM, and the effects of the transfer process were also determined by TEM analysis. Chemical structures of polymer thin films were revealed by FTIR analysis. The cell efficiency of the graphene-based alternative counter electrodes produced was determined by a solar simulator.

Results and discussions

Structural and morphological properties of TNT arrays

SEM images of TiO_2 nanotubes at different magnifications are given in Fig. 2. From SEM images, it is clear that the average nanotubes diameter of the TNT arrays is about 90.3 nm. The inner and outer diameter of nanotube was found as 89.8 nm and 130.2 nm, respectively (shown by red lines in Fig. 2a). The average wall thickness of TNTs was 40 nm. In addition, the average length of the nanotubes was approaximately 2.5 μm (Fig. 2d). One-dimensional (1D) TiO_2 nanostructures can offer faster electron transport and higher electron mobility than TiO_2-nanoparticle films. This is because the morphological structure can significantly reduce electron scattering from the grain boundaries. In this way, the photoexcited electron mobilizes through the semiconductor film with lower transport time, and the recombination and electron lifetime is reduced. As a result, in the literature, uniform TNT arrays growth was carried out by the anodization of titanium in fluorine-based solutions, and the nanotubes had diameters of 20 to 110 nm, lengths of 0.2 to 4 μm and wall thickness of 7–40 nm [29, 30]. In this study, the diameters, lengths and wall thickness of nanotubes grown by anodization method are in good agreement with the literature [20].

Structural, optical and morphological properties of CVD-grown graphene

Raman spectroscopy was used to examine the structural properties of CVD graphene and was presented in Fig. 3a. Positions of G and 2D characteristic peaks of graphene film were determined as approximately 1582 and 2689 cm^{-1}, respectively. The $I_{(2D)}/I_{(G)}$ intensity ratio, which is one of the Raman parameters to help determine the number of layers of the film, was calculated as approximately 2.3. The other parameter is the full width at half maximum of the 2D peak $(FWHM)_{2D}$ and is approximately 36.5 cm^{-1} for the film used in this study. The positions of the G and 2D peaks, $I_{(2D)}/I_{(G)}$ intensity ratio and (FWHM)
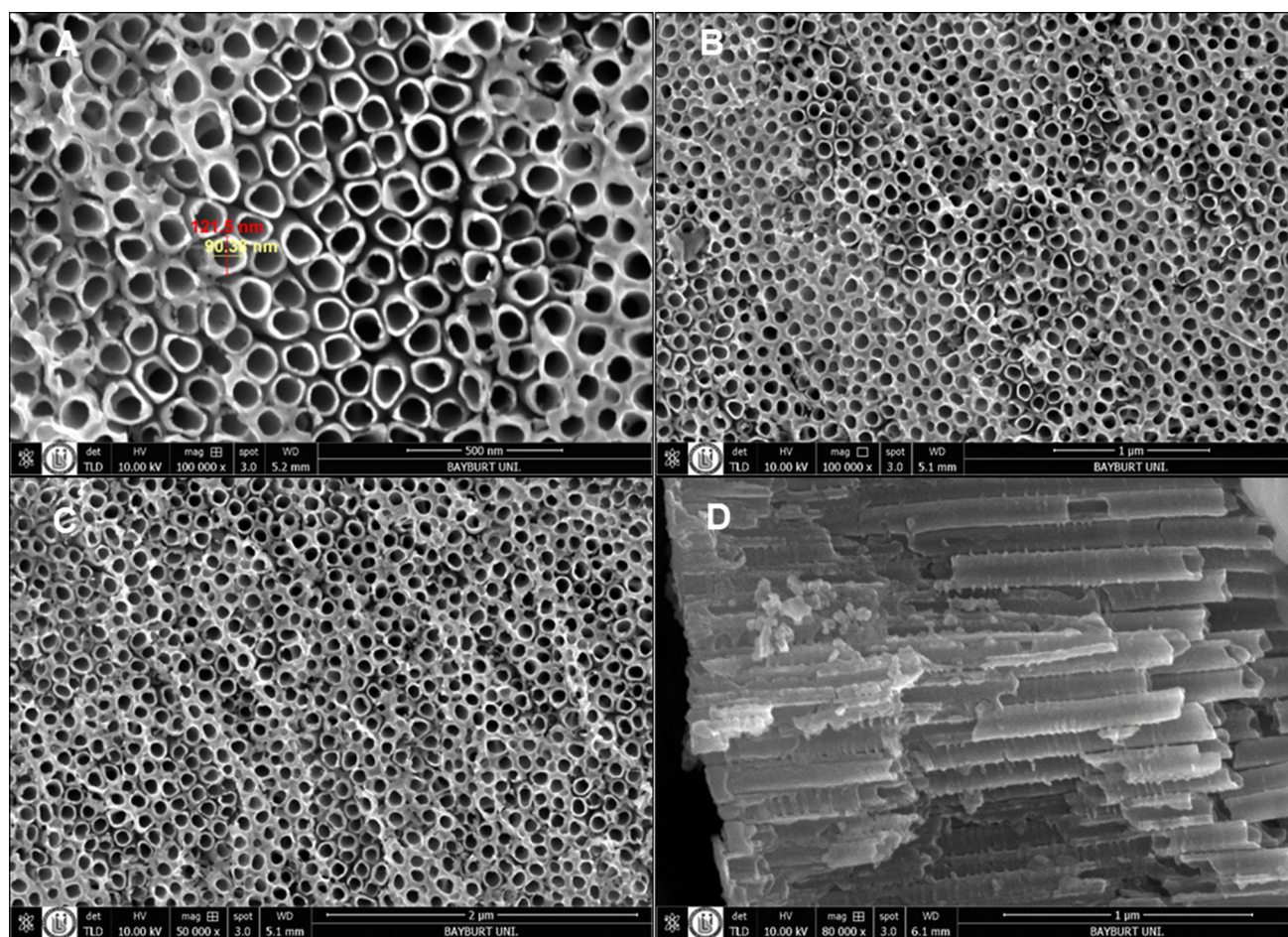
Figure 2 SEM images of TNTs at different magnifications.

$_{2D}$ value clearly show that the film is a single-layer graphene [23, 31, 32]. To determine the optical properties, UV–Vis spectroscopy was performed to the graphene transferred on the glass. As can be seen in Fig. 3b, the optical transmittance of graphene is ∼97.5% at 550 nm, which is in good agreement with that of the monolayer graphene in previous studies [33–35]. Moreover, the morphological features and the number of layers of the graphene transferred onto the copper TEM grid were revealed by TEM and the TEM images, and the selected area electron diffraction SAED pattern is shown in Fig. 3c and d (inset). The SAED pattern (Fig. 3d) clearly reveals the hexagonal crystalline structure of CVD-grown graphene film. TEM images confirm that the graphene film is a single-layer (blue lines and arrows) and shows that it contain folded edges (red lines and arrows), wrinkles (yellow arrows) and few layer graphene domains (purple arrows). TEM images of Fig. 3c and d, presented at 500 nm and 200 nm,

respectively, were taken to reveal the presence of both the monolayer graphene structure and the defects occurring in the transfer process. In Fig. 3 c and d, the graphene monolayer line is clearly visible (arrows marked in blue). In addition, the part where the single-layer folded is shown with red arrows. However, wrinkles in the morphological structure were also tried to be shown with yellow arrows. The 2D peak was taken on a smaller scale to demonstrate the presence of possible organic residues occurring in the graphene transfer process. The presence of polymeric and organic residues such as PMMA was detected in the regions indicated by green arrows [36]. However, with the purple arrows, it was determined that the black dots were graphene particles with one or more layers [37].
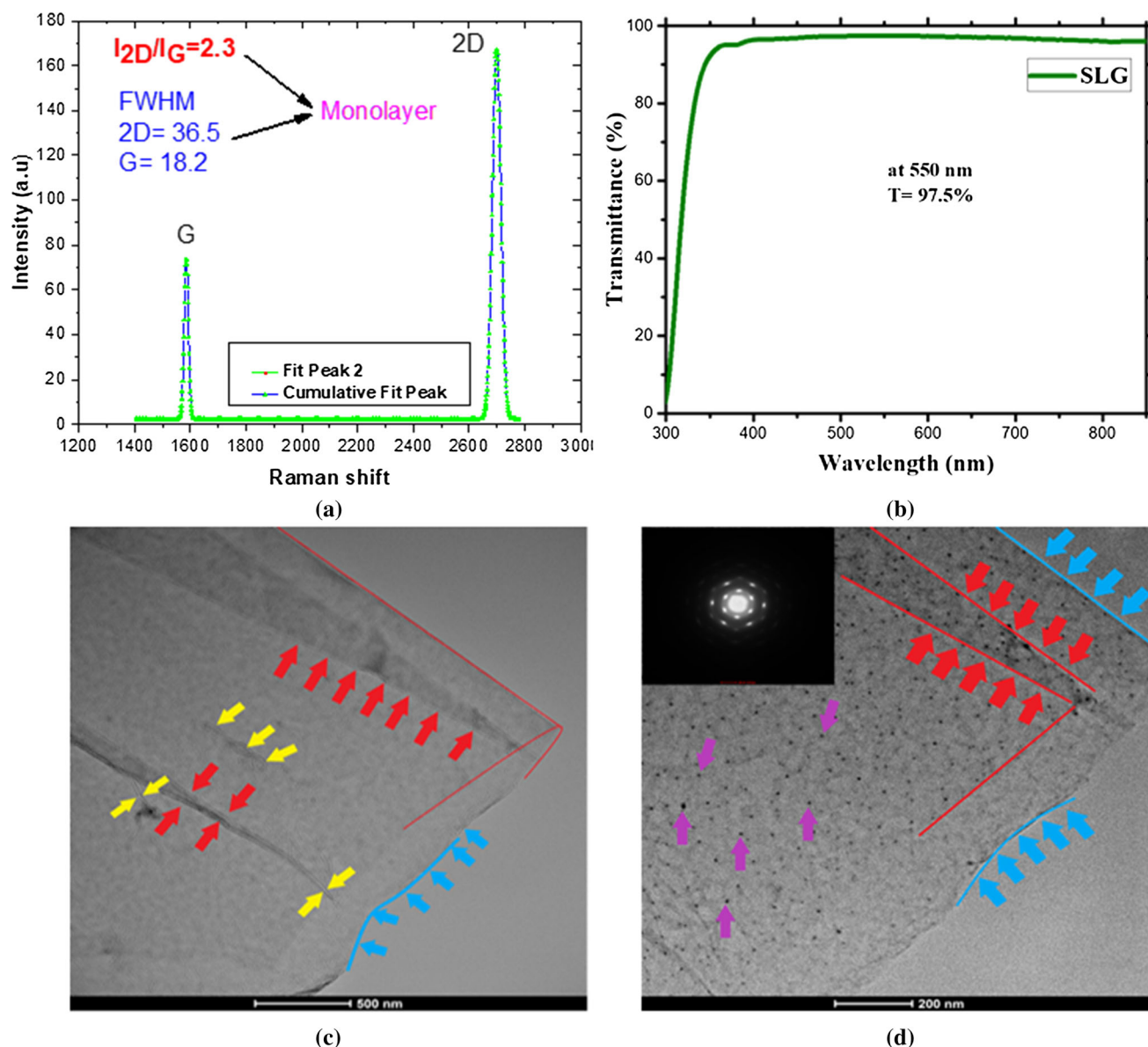
Figure 3 a Raman spectrum, **b** UV–Vis spectrum, **c** TEM images of CVD graphene **d** TEM image and SAED pattern (inset) of CVD-grown graphene.

Chemical structure analysis of polymers

To investigate the chemical composition and determine the functional groups, FTIR spectra of the liquid monomers and plasma polymerized thin films were recorded and are given in Figs. 4, 5 and 6 in FTIR spectrum of D-Limonene monomer (Fig. 4), the absorption bands at about 3085 and 3012 cm^{-1} can be attributed to the stretching of unsaturated C–H bonds. Four strong bands located at 2965, 2921, 2855 and 2836 cm^{-1} can be assigned to the asymmetric stretching and symmetric stretching of C–H bonds of D-Limonene monomer [38, 39][. The peak with medium intensity centered at 1731 cm^{-1} represents the C=O vibrations [39]. Four of the main characteristic bands of Limonene which is main component of grapefruit, orange and bitter orange oils observed at 1644, 1453, 1436 and 886 cm^{-1} are attributed to stretching of unsaturated C=C bonds, asymmetric bending of C–H, symmetric bending of C–H, out-of-plane bending of C–H, respectively [40]. Additionally, the medium intensity peaks founded at 1376 and 797 cm^{-1} correspond to symmetric bending of C–H and out-of-plane bending, respectively [41].
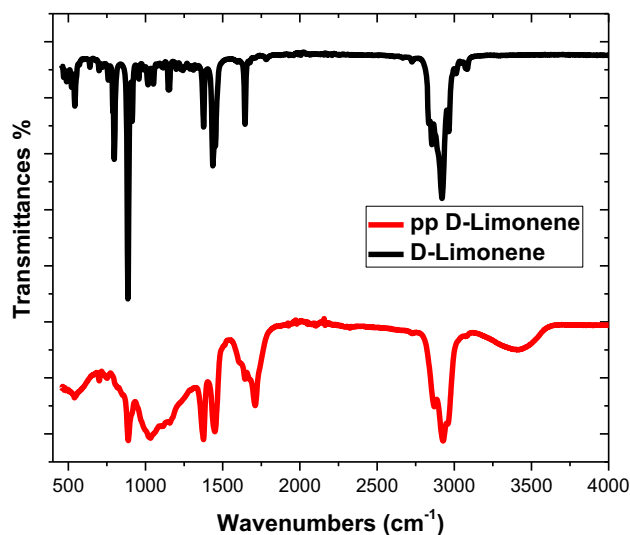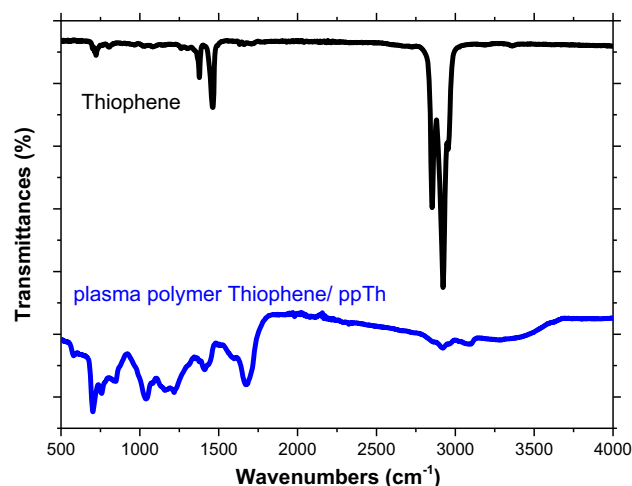
Figure 4 FTIR spectra of monomer (top spectrum) and polymer (bottom spectrum).
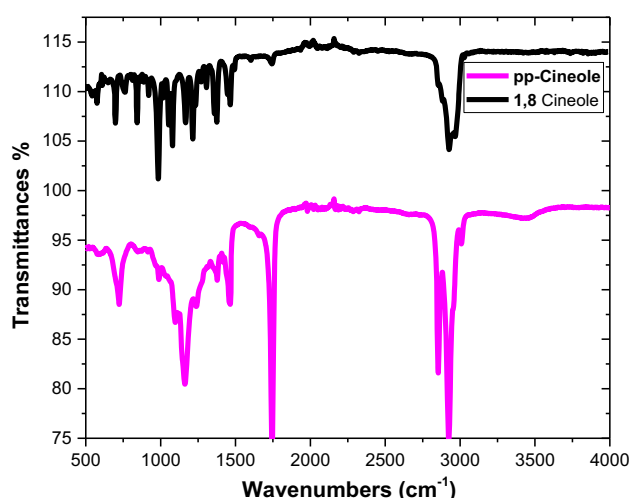
Figure 5 FTIR spectra of monomer (top spectrum) and polymer (bottom spectrum).

Compared to the monomer in terms of vibrational properties, it is clear that in the spectrum of the plasma polymerized film, the intensity of some bands was reduced and some bands disappeared after the plasma polymerization process. However, several new peaks have emerged which are attributed to the stretching of the hydroxyl group (3450 cm^{-1}), C=O bonds (1710 cm^{-1}) and C–O bonds (between 1150 and 1000 cm^{-1}) [42]. These bands, which indicate the presence of hydroxyl and carboxyl groups, may be due to the bonding of free radicals with oxygen in the air in films obtained from essential oils [41, 43] and the presence of these groups is thought to enhance

Figure 6 FTIR spectra of monomer (top spectrum) and polymer (bottom spectrum).

the photocatalytic performance of the counter electrode [31]. In FTIR spectrum of plasma polimerized thin film (ppLim), strong bands observed at 2957 and 2927 cm^{-1} are attributed to the asymmetric stretching of C–H bonds in methyl group. The symmetric stretching of C–H was observed at 2871 cm^{-1} [39, 41], to weaker than its asymmetric stretching. There are also different intense bands corresponding to asymmetric (1450 cm^{-1}) and symmetric stretching of C–H bonds (1376 cm^{-1}), out-of-plane bending of unsaturated C–H bonds (888 cm^{-1}) and stretching of unsaturated C=C bonds (1644 cm^{-1}) in FTIR spectrum of ppLim [30, 39, 40].

In the spectrum of the 1,8-cineol monomer (Fig. 5), there are many characteristic bands which indicate asymmetric (2966 and 2926 cm^{-1}) and symmetric stretching of the C–H groups (2883 and 2854 cm^{-1}) [44] as well as the bending of the C–H groups (1465, 1446, 1375, 1080 and 1053 cm^{-1}) [44]. The bands corresponding to the stretching of the C–C bonds are observed at 1360, 1306, 1271 and 1215 cm^{-1}. The band at 1167 cm^{-1} corresponds to stretching of the C–O groups [44]. In addition, strong or weak bands located at 1016, 984, 920, 843, 812, 763 and 574 cm^{-1} are assigned to deformation vibrations of C–H [25, 44, 45]. After plasma treatment, although some functional groups in the monomer maintain in plasma polymerized film, it is obvious that the intensity of some bands, especially in the fingerprint region, has decreased. In spectrum of ppCin, the bands at 2924 and 2854 cm^{-1} represent the C-H stretch vibrations (asymmetric and symmetric,

respectively) [44]. The peaks at 1465 and 1378 cm^{-1} are attributed to in-plane C–H bending of ring structure while the peaks at 1240, 1162 and 988 cm^{-1} to C–C stretch vibration, C–O bending and C–H deformation, respectively [45, 46]. For all that, the broad and weak peak at 3450 cm^{-1} indicates the presence of hydroxyl group and also strong peak at 1745 cm^{-1} represents carbonyl groups of ester [45]. Disappearance or reduce intensity of characteristic peaks (C–C and C–H bending) may be proof that the polymer film is highly crosslinked [46].

The IR absorption spectra of thiophene and polythiophene (ppTh), (Fig. 6) shows the following most important peaks: O–H stretching (3250 cm^{-1}, not present in the monomer) [32], C–H stretching of thiophene ring (3100 cm^{-1}), aliphatic C-H asymmetric stretching of methyl and methylene (2964 and 2923 cm^{-1}, respectively), aliphatic C-H symmetric stretching of methylene (2853 cm^{-1}) [47], aromatic C=C asymmetric and symmetric stretching (1675 and 1432 cm^{-1}, respectively) [47, 48], out-of-plane bending of C-H (845 cm^{-1}) [48] and C-H bending of thiophene ring (701 cm^{-1}) [47, 48]. The presence of the bands belonging to the thiophene ring in the polymer during the plasma polymerization process points out that the chemical structure is still preserved.

Photovoltaic performances of functionalized of CVD-grown graphene as counter electrodes in dye-sensitized solar cells

The photocurrent density (J) versus photovoltage (V) curves of DSSCs using TNT arrays photoanodes and functionalized of SLG with different polymers CEs are represented in Figs. 7 and 8. Also, their photovoltaic parameters such as short-circuit current density (J_{SC}), short-circuit current (I_{SC}), open-circuit voltage (V_{OC}), fill factor (FF) and efficiency of DSSCs (η) are given in Table 1. The SLG counter electrode showed J_{SC} of 0.16 mAcm^{-2}, I_{SC} of 0.03 mA, V_{OC} of 0.522 V, FF (%) of 58.7 and η of 0.02%, which are entirely low and inevitable (Fig. 7). This is due to the fact that although the SLG has high charge mobility in plane, its basal plane naturally reduces charge mobility at the graphene/electrolyte interface. Furthermore, its perfect crystal structure has a relatively few number of electrocatalytic active sites containing defects necessary for the reduction of the iodide/triode solution [49, 50]. When SLG was functionalized
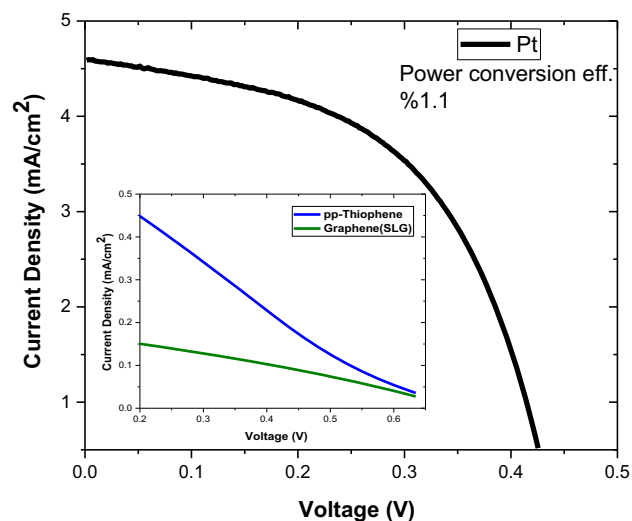
Figure 7 J-V characteristic curves of DSSCs based on Pt, SLG and pp-(Thiophene)/SLG counter electrodes.
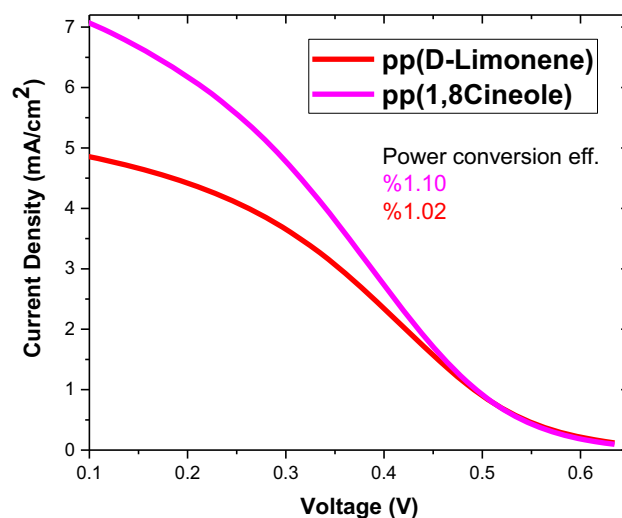
Figure 8 J-V characteristic curves of DSSCs based on graphene/polymer (D-Limonene and 1,8-cineole) counter electrodes.

with D-Limonene and used as a counter electrode in a DSSC, ppLim/SLG CE exhibited J_{SC} value of 7.18 mAcm^{-2}, I_{SC} value of 1.41 mA, V_{OC} value of 0.610 V, FF (%) value of 46.0 and η value of 1.02% (Fig. 8). The Jsc, Isc, V_{OC}, FF (%) and η values of ppCin/SLG were calculated as 5.16 mAcm^{-2}, 0.99 mA, 0.695 V, 58.9 and 1.10%, respectively. When SLG is functionalized with an aromatic polymer or organic molecule according to the surface non-covalent approach, interaction between basal plane of SLG and their π systems is achieved through van der Waals forces or π–π interaction. SLG and these polymers (D-Limonene or 1,8-cineol) have an

Table 1 Photovoltaic performance parameters of DSSCs based on counter electrodes

Counter electrode	V_{OC} (V)	I_{sc} (mA)	J_{sc} (mA/cm^2)	FF (%)	η (%)
SLG/ppCin	0.695	0.99	5.16	58.9	1.10
SLG/ppLim	0.610	1.41	7.18	46.0	1.02
SLG/ppTh	0.509	0.09	0.46	40.8	0.05
Gr (SLG)	0.522	0.03	0.16	58.7	0.02
Pt (Çırak et al. [20])	0.440	–	4.60	53.0	1.10

aromatic and planar six-membered ring geometry, which required for a strong π–π interaction between the two components [51]. Thus, the charge mobility between the CE/electrolyte and SLG/polymer interfaces and also the electrocatalytic activity of the CE is enhanced. As a result photovoltaic parameters (J_{SC}, V_{OC}, η etc.) are reasonably increased that of SLG. This situation is also supported by charge transfer resistances according to EIS results. In the previous study performed by Çırak et al. [20], DSSC consisting of TNT nanotubes photoanode obtained with the same anodization parameters and PtCE showed J_{SC} of 4.60 mAcm^{-2}, V_{OC} of 0.44 V, FF (%) of 53.0 and η of 1.1%. The J_{SC} and V_{OC} values of both ppCin/SLG and ppLim/SLG CEs were higher, while the η values were approximately equal to those of PtCE. But, charge transfer resistances of fuctionalization SLG are still high, and also FF is low according to PtCE. Further, ppTh/SLG counter electrode exhibited a worse photovoltaic performance than ppCin/SLG and ppLim/SLG. This may be due to the five-membered ring structure of Thiophene.

Electrochemical impedance spectroscopy (EIS) was performed to investigate the electrochemical properties of DSSCs using non-covalent functionalized graphene as counter electrodes. The Nyquist plots and the equivalent circuit of the DSSCs are demonstrated in Fig. 9. The parameters obtained by fitting the EIS data from the equivalent circuit, wherein R_s, R_{CT1}, R_{CT2}, CPE, and Z_n indicate the series resistance, the charge transfer resistance at the photoanode interface, the charge transfer resistance at the counter electrode/electrolyte interface, the capacitive constant phase at the interface and the Warburg diffusion impedance, respectively [20]. Rs is a measure of the conductivity of the counter electrode and represents the contact resistance between the carbonaceous structure and the FTO substrate. Rs is the resistance value between the point where the semicircle intersects on the actual axis and the origin in the high frequency region (> 1000 Hz) [52]. Typically, the
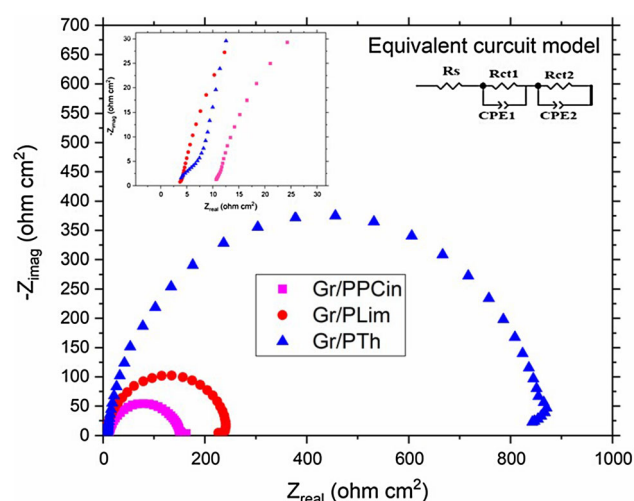
Figure 9 Nyquist plots of EIS spectra of DSSCs based on graphene-graphene/polymers counter electrodes.

Nyquist plots are composed of three semicircles, the first (R_{CT1}) and second (R_{CT2}) ones are represented the charge transfer and charge recombination resistance at the TiO$_2$/dye/electrolyte and CE/electrolyte interfaces, while the third one is related to Warburg diffusion process of iodide/triodide electrolyte solution [53]. However, when a graphene-based counter electrode is used in DSSCs, the electron transfer frequency at the CE/electrolyte interface (medium frequency region) is very close to that of the TiO$_2$/dye/electrolyte interface (low frequency region). Hence, the first and second semicircles overlap and disappear partially or completely in Nyquist plots [54]. This is also seen in this study (Fig. 9 inset) and the charge transfer resistance at the functionalized SLG/electrolyte interface is indicated as R_{CT}.

The Rs value of SLG is 51.23 Ωcm^2. When SLG was functionalized, the Rs values of ppTh/SLG, ppLim/SLG and ppCin/SLG were 3.49 Ωcm^2, 3.10 Ω cm^2 and 10.52 Ωcm^2, respectively, and were significantly reduced compared to that of SLG. These Rs results show that non-covalent functionalization of SLG with d-limonene, 1,8-cineol and thiophene increased

conductivity compared with SLG. Although the R_{CT} value of SLG was 1519 Ωcm^2, the R_{CT} value of pTh/SLG, ppLim/SLG and ppCin/SLG decreased to 870.5 Ωcm^2, 283.9 Ωcm^2 and 134.1 Ωcm^2, respectively. This clearly shows that non-covalent functionalization of SLG with polymers (especially, d-limonene and 1,8-Cineol) by plasma polymerisation reasonably improved the electron transfer mechanism and electrocatalytic activity, and thus increased photovoltaic parameters compared to those of SLG. In addition, the CPE values of SLG, pTh/SLG, ppLim/SLG and ppCin/SLG, respectively, are 32.30 µF, 19.22 µF, 14.78 µF and 6.60 µF, which are a measure of specific large surface area and electrocatalytic activity. For better interaction of I_3^- with the counter electrode and reduction of the redox solution, the functionalization of SLG provided higher number of electrochemical active sites [52, 55]. At the same time, functional groups such as carboxyl and hydroxyl, which have oxygen as a result of SLG functionalization, may have caused the defective areas necessary for further interaction of the triodide ions. Compared to PtCE, it may seem a contradiction that ppLim/SLG and ppCin/SLG CE also have higher Jsc values, although they have higher R_{CT} values. This phenomenon is thought to cause the J-V curves to bend near the Voc values and it is normally seen in graphene-based counter electrodes. Although the electron transfer rate at electrode/electrolyte interface is slow for the graphene-based counter, it is fast at the PtCE/electrolyte interface. Due to the dense morphological structure of the Pt thin film, the diffusion and penetration of iodide/triiodide redox couples into the depths may be limited. However, the morphological structure of the graphene/polymer CE may allow more redox couples to interact and collect more photocurrent than PtCE. Roy-Mayhew et al. reported that a polymer thermally reduced graphene oxide (TRGO) composite showed 5% photovoltaic performance and that the functional groups of the polymer and defects had an important role for catalysis [12]. Kim et al. interpreted the superior electrocatalytic activity of the carbon-based counter electrode they produced to active sites attributed to defects and functional groups [56].

The cell efficiencies of our graphene-based electrodes were also compared with some previously reported studies. Hong et al. [57] applied grafene/PEDOT-PSS composite films with graphene and polystyrene fluoride as counter electrodes of DSSCs.

These counter electrodes showed high transmittance (> 80%) at 550 wavelengths and high electrocatalytic activity. The power conversion efficiency of DSSC was 4.5%, and the cell efficiency of platinum synthesized under the same experimental condition was 6.3%. It is explained by the large surface area and chemical defects of graphene that positively affect the catalytic activity of the iodine [58]. The conductive matrix structure of the PEDOT/graphene structure caused also an improvement on cell efficiency. Shadid et al. used the hybrid structure consisting of PANI films grown by polymerization technique on graphene thin films as a counter electrode in DSSC. Although this hybrid structure significantly increased the catalytic activity of the electrolyte, its power conversion efficiency was found to be lower (3.58%) than the Pt (3.97%) electrode due to its high charge transfer resistance [18]. Although there are many new generation counter electrodes produced as an alternative to the Pt electrode in the literature, most of them are not yet superior to the power conversion efficiency of the Pt electrode. In our study, the synthesized polymer functionalized graphene, especially those obtained from essential oil components, showed better photovoltaic performance than the Pt electrode and it is also the first because they are environmentally friendly electrodes. The most important insufficiency of our study is that the power conversion efficiency of DSSC is restricted because TNT photoanodes are not optically transparent. The efficiency of the Pt electrode, which has a cell efficiency of around 11% today, is very low for our study. Therefore, it is thought that if optically transparent photoanote is used, the efficiency of the DSSC can be improved further.

Conclusions

In summary, SLG films were functionalized using noncovalent approach with 1,8-cineole, D-Limonene and thiophene, respectively. SLG and polymer functionalized SLGs were used as counter electrodes in DSSCs, and the effect of functionalized SLGs on the photovoltaic parameters of DSSCs was investigated. DSSCs with ppCin/SLG, ppLim/SLG and ppTh/SLG CEs exhibited η of 1.10%, 1.02%, 0.05% and J_{SC} of 5.16, 7.18, 0.46 $mAcm^{-2}$, respectively and were considerably higher than those of SLG electrode (η = 0.02%, J_{SC} = 0,06 $mAcm^{-2}$). The SLG counter

electrode showed poor photovoltaic performance, but polymer functionalized SLG counter electrode offered a remarkable increase in photovoltaic performance as a result of significantly improved electrical conductivity and electrocatalytic activity. The results obtained from photovoltaic analysis show that aromatic and hexagonal structure of graphene and polymers can improve their electrical and electrocatalytic activity properties by making non-covalent bonds between them. As a result of the functionalization of SLG with three polymers, all of them exhibit better photovoltaic performance than SLG, while ppLim/SLG and ppCin/SLG have very close photovoltaic performance with that of PtCE. Although the Jsc, Isc and Voc values of the ppLim/SLG and ppCin/SLG CEs were higher than those of PtCE, they have higher R_{CT} and Rs values caused the cell efficiency to decrease.

Acknowledgements

References

[1] O'reganGrätzel BM (1991) A low-cost, high-efficiency solar cell based on dye-sensitized colloidal TiO 2 films. Nature 353(6346):737–740

[2] Yu F et al (2019) A new breakthrough for graphene/carbon nanotubes as counter electrodes of dye-sensitized solar cells with up to a 10.69% power conversion efficiency. J Power Sour 412:366–373

[3] Wu W-T et al (2016) Study of graphene nanoflake as counter electrode in dye sensitized solar cells. Diam Relat Mater 65:91–95

[4] Zhang S et al (2019) Increased power conversion efficiency of dye-sensitized solar cells with counter electrodes based on carbon materials. RSC Adv 9(38):22092–22100

[5] Wu M et al (2011) Two flexible counter electrodes based on molybdenum and tungsten nitrides for dye-sensitized solar cells. J Mater Chem 21(29):10761–10766

[6] Wu M et al (2012) Economical Pt-free catalysts for counter electrodes of dye-sensitized solar cells. J Am Chem Soc 134(7):3419–3428

[7] Gong F et al (2012) In situ growth of Co0 85Se and Ni0 85Se on conductive substrates as high-performance counter electrodes for dye-sensitized solar cells. J Am Chem Soci 134(26):10953–10958

[8] Singh E et al (2017) Two-dimensional transition metal dichalcogenide-based counter electrodes for dye-sensitized solar cells. RSC Adv 7(45):28234–28290

[9] Tang Z, Zhuang J, Wang X (2010) Exfoliation of graphene from graphite and their self-assembly at the oil− water interface. Langmuir 26(11):9045–9049

[10] Singh E, Nalwa HS (2015) Graphene-based dye-sensitized solar cells: a review. Sci Adv Mater 7(10):1863–1912

[11] Guo X, Lu G, Chen J (2015) Graphene-based materials for photoanodes in dye-sensitized solar cells. Front Energy Res 3:50

[12] Roy-Mayhew JD et al (2010) Functionalized graphene as a catalytic counter electrode in dye-sensitized solar cells. ACS Nano 4(10):6203–6211

[13] Li R et al (2016) Counter electrodes from conducting polymer intercalated graphene for dye-sensitized solar cells. J Power Sour 309:231–237

[14] Hsu Y-C, Chen G-L, Lee R-H (2014) Graphene oxide sheet-polyaniline nanocomposite prepared through in-situ polymerization/deposition method for counter electrode of dye-sensitized solar cell. J Polym Res 21(5):440

[15] He B et al (2014) Robust polyaniline–graphene complex counter electrodes for efficient dye-sensitized solar cells. ACS Appl Mater Interfaces 6(11):8230–8236

[16] Sun W et al (2013) Hierarchically porous hybrids of polyaniline nanoparticles anchored on reduced graphene oxide sheets as counter electrodes for dye-sensitized solar cells. J Mater Chem A 1(8):2762–2768

[17] Wang M et al (2014) Counter electrodes from polyaniline−graphene complex/graphene oxide multilayers for dye−sensitized solar cells. Electrochim Acta 137:175–182

[18] Shahid MU et al (2019) Few-layer graphene supported polyaniline (PANI) film as a transparent counter electrode for dye-sensitized solar cells. Diam Relat Mater 94:242–251

[19] Lee KS et al (2012) Flexible and platinum-free dye-sensitized solar cells with conducting-polymer-coated graphene counter electrodes. Chemsuschem 5(2):379–382

[20] Çırak BB et al (2017) Synthesis, surface properties, crystal structure and dye sensitized solar cell performance of TiO2 nanotube arrays anodized under different voltages. Vacuum 144:183–189

[21] Kaymak N, Bayram O, Tataroglu A, Ocak SB, Orhan EO (2020) Electrical properties of graphene/silicon structure

with Al$_2$O$_3$ interlayer. J Mater Sci Mater Electron. https://doi.org/10.1007/s10854-020-03517-1

[22] Ibrahim A et al (2017) Study of the impact of chemical etching on Cu surface morphology, graphene growth and transfer on SiO2/Si substrate. Carbon 123:402–414

[23] Bayram O, Simsek O (2019) Vertically oriented graphene nano-sheets grown by plasma enhanced chemical vapor deposition technique at low temperature. Ceram Int 45(11):13664–13670

[24] Ouyang B, Zhang Y, Zhang Z, Fan HJ, Rawat RS (2016) Green synthesis of vertical graphene nanosheets and their application in high-performance supercapacitors. RSC Advances 6(28):23968–23973

[25] Bayram O, Simsek O (2018a) A study on the optical, chemical and dielectric properties of PPCIN thin films derived from essential oil compounds using RF plasma polymerisation technique. Vacuum 156:198–204

[26] Bayram O, Simsek O (2018b) Investigation of the effect of RF energy on optical, morphological, chemical and antibacterial properties of PolyTerpenol thin films obtained by RF-PECVD technique. J Mater Sci Mater Electron 29(8):6586–6593. https://doi.org/10.1007/s10854-018-8642-y

[27] Cakmak K et al (2019) Plasma polymerized linalool (ppLin): an antimicrobial and biocompatible coating. Turk J Chem 43(1):323–334

[28] Bayram O (2018a) Conjugated polythiophene/Ni doped ZnO hetero bilayer nanocomposite thin films: its structural, optical and photoluminescence properties. Ceram Int 44(17):20635–20640

[29] Kang SH et al (2008) Columnar rutile TiO2 based dye-sensitized solar cells by radio-frequency magnetron sputtering. J Power Sour 184(1):331–335

[30] Marien CB et al (2016) TiO2 nanotube arrays: influence of tube length on the photocatalytic degradation of paraquat. Appl Catal B 194:1–6

[31] Li X et al (2009) Large-area synthesis of high-quality and uniform graphene films on copper foils. Science 324(5932):1312–1314

[32] Hao Y et al (2010) Probing layer number and stacking order of few-layer graphene by Raman spectroscopy. Small 6(2):195–200

[33] Nair RR et al (2008) Fine structure constant defines visual transparency of graphene. Science 320(5881):1308–1308

[34] Pekdemir S, Onses MS, Hancer M (2017) Low temperature growth of graphene using inductively-coupled plasma chemical vapor deposition. Surf Coat Technol 309:814–819

[35] Bayram O (2019) A study on 3D graphene synthesized directly on glass/FTO substrates: Its Raman mapping and optical properties. Ceram Int 45(14):16829–16835

[36] Kalita D (2015) Graphene produced by chemical vapor deposition: from control and understanding of atomic scale defects to production of macroscale functional devices (Doctoral dissertation)

[37] Panthani MG et al (2012) Graphene-supported high-resolution TEM and STEM imaging of silicon nanocrystals and their capping ligands. J Phys Chem C 116(42):22463–22468

[38] Coates J (2006) Interpretation of Infrared spectra, a practical approach. In: Encyclopedia of Analytical Chemistry. https://doi.org/10.1002/9780470027318.a5606

[39] Alancherry S, Bazaka K, Jacob MV (2018) RF plasma polymerization of orange oil and characterization of the polymer thin films. J Polym Environ 26(7):2925–2933

[40] Schulz H et al (2002) Quantitative analysis of various citrus oils by ATR/FT-IR and NIR-FT Raman spectroscopy. Appl Spectrosc 56(1):117–124

[41] Gerchman D et al (2019) Thin film deposition by plasma polymerization using d-limonene as a renewable precursor. Prog Org Coat 129:133–139

[42] Bazaka K, Jacob MV (2010) Post-deposition ageing reactions of plasma derived polyterpenol thin films. Polym Degrad Stab 95(6):1123–1128

[43] Friedrich J (2011) Mechanisms of plasma polymerization–reviewed from a chemical point of view. Plasma Process Polym 8(9):783–802

[44] Bayram O (2018b) Determination of the optical and chemical properties of aniline doped plasma polymerized cineole thin films synthesized at various RF powers. J Mater Sci Mater Electron 29(10):8564–8570

[45] Easton CD, Jacob MV, Shanks RA (2009) Fabrication and characterisation of polymer thin-films derived from cineole using radio frequency plasma polymerisation. Polymer 50(15):3465–3469

[46] Sakthi Kumar D et al (2003) Electrical and optical properties of plasma polymerized eucalyptus oil films. J Appl Polym Sci 90(4):1102–1107

[47] Satulu V et al (2010) Polymer-like thin films obtained by RF plasma polymerization of pentacyclic monomers. J Optoelectron Adv Mater 12(3):631

[48] Vassallo E et al (2007) Characterization of Poly (3-Methylthiophene)-like Films Produced by Plasma Polymerization. Plasma Process Polym 4(S1):S801–S805

[49] Rahman MS et al (2016) Prospects of conducting polymer and graphene as counter electrodes in dye-sensitized solar cells. J Polym Res 23(9):192

[50] Saranya K, Rameez M, Subramania A (2015) Developments in conducting polymer based counter electrodes for dye-sensitized solar cells–An overview. Eur Polym J 66:207–227

[51] Georgakilas V et al (2016) Noncovalent functionalization of graphene and graphene oxide for energy materials,

biosensing, catalytic, and biomedical applications. Chem Rev 116(9):5464–5519

[52] Zhao J et al (2016) Application of non-covalent functionalized carbon nanotubes for the counter electrode of dye-sensitized solar cells. Org Electron 30:52–59

[53] Ahmad I et al (2014) Carbon nanomaterial based counter electrodes for dye sensitized solar cells. Sol Energy 102:152–161

[54] Hung K-H, Li Y-S, Wang H-W (2012) Dye-sensitized solar cells using graphene-based counter electrode. in 2012 12th IEEE International Conference on Nanotechnology (IEEE-NANO)

[55] Velten J et al (2012) Carbon nanotube/graphene nanocomposite as efficient counter electrodes in dye-sensitized solar cells. Nanotechnology 23(8):085201

[56] Kim H et al (2012) Fabrication and characterization of carbon-based counter electrodes prepared by electrophoretic deposition for dye-sensitized solar cells. Nanoscale Res Lett 7(1):53

[57] Hong W et al (2008) Transparent graphene/PEDOT–PSS composite films as counter electrodes of dye-sensitized solar cells. Electrochem Commun 10(10):1555–1558

[58] Trancik JE, Barton SC, Hone J (2008) Transparent and catalytic carbon nanotube films. Nano Lett 8(4):982–987